

A review of selected techniques for characterizing radiation-induced defects in solar cells

A. Rohatgi, J. P. Schaffer, G. Augustine and M. S. Ramanachalam

Georgia Institute of Technology, Atlanta, GA 30332 (U.S.A.)

Abstract

A review of three promising defect characterization techniques is presented. It is shown how deep level transient spectroscopy can provide information about energy level, density and capture cross-section of electrically active defects produced by irradiation. Both Doppler and lifetime positron annihilation spectroscopies are reviewed to show how configuration of radiation-induced defects can be identified by these techniques. Finally, the electron paramagnetic resonance technique is briefly reviewed and its usefulness is demonstrated by describing the investigations of radiation-induced Si-A center and positively charged silicon vacancy defect.

1. Introduction

Silicon photovoltaic arrays are the major source of spacecraft electric power today. GaAs solar cells are beginning to see limited use in space applications where end-of-life array output power in a radiation environment is a major design consideration [1]. Recently, InP solar cells have become a promising candidate for future space power applications because of their superior radiation tolerance, annealing characteristics [2] and potential for high efficiency which has already reached $\approx 19\%$ at air mass (AM)0 [3]. It is conceivable that all three types of cell will eventually be used in space depending on the power requirements and radiation environment. In addition to the material, radiation tolerance is also a function of cell configuration. At present, n^+p cell configuration is preferred exclusively over p^+n configuration [4] for silicon cells because of demonstrated superior radiation resistance. For GaAs and InP, it is somewhat unclear which configuration is better because of scarcity of data and lack of detailed characterization of defects and their annealing behavior. Limited data in the literature suggest that the p^+n configuration is more radiation resistant for GaAs, but that the n^+p configuration has the edge in the InP cells.

Various materials and cell configurations respond differently to the same radiation environment because of differences in the radiation-induced defects or recombination centers. The extent to which these recombination centers or traps degrade the minority carrier lifetime and solar cell performance depends upon the density, capture cross-section and location of the defect state within the bandgap of the semiconductor. Thus, in order to understand

the difference in the radiation tolerance of various solar cells, one needs to determine the defect configuration, trap parameters and annealing characteristics of the defects. The objectives of this paper are (1) to review some of the important and popular techniques used to characterize radiation-induced defects in semiconductors, and (2) to show how a combination of these techniques can be used to delineate, identify and understand the radiation-induced defects and their annealing characteristics in silicon, GaAs and InP solar cells. In this review article, we have used selected information from the literature along with our own data to illustrate the application of characterization techniques described in this paper.

2. Assessment of radiation damage by solar cell measurements

A solar cell is an excellent device to assess the magnitude of radiation damage and establish the superiority of a material or cell configuration. Based on normalized cell efficiency and cell output power, after proton radiation, Weinberg *et al.* [5] were able to show clearly that radiation resistance of InP solar cells is superior to both GaAs and silicon (See Fig. 1). Internal spectral response is another popular cell measurement technique used to quantify the extent of radiation damage. In this technique, short circuit current is measured at each wavelength and internal quantum efficiency (number of electrons collected per photon) is plotted as a function of wavelength. From the decrease in internal quantum efficiency, it is possible to calculate the change in minority carrier diffusion length [6]. It is also possible to assess the radiation-induced change in minority carrier diffusion length and surface recombination velocity by matching the measured and calculated spectral response using a solar cell computer modeling code like PC-ID [7]. In Fig. 2, we show the match in the measured and calculated spectral response, as well as the cell data, for an n^+p InP solar cell, before and after irradiation with 10 MeV protons with a fluence of $2 \times 10^{13} \text{ cm}^{-2}$. Using this methodology, we are able to show that the above proton radiation decreases the bulk lifetime from 0.75 to 0.028 ns, while the front surface recombination velocity is essentially unchanged. The accuracy of this meth-

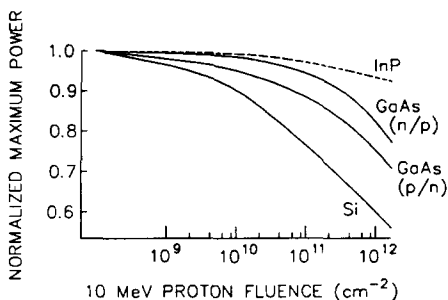


Fig. 1. Normalized output power as a function of proton fluence [15].

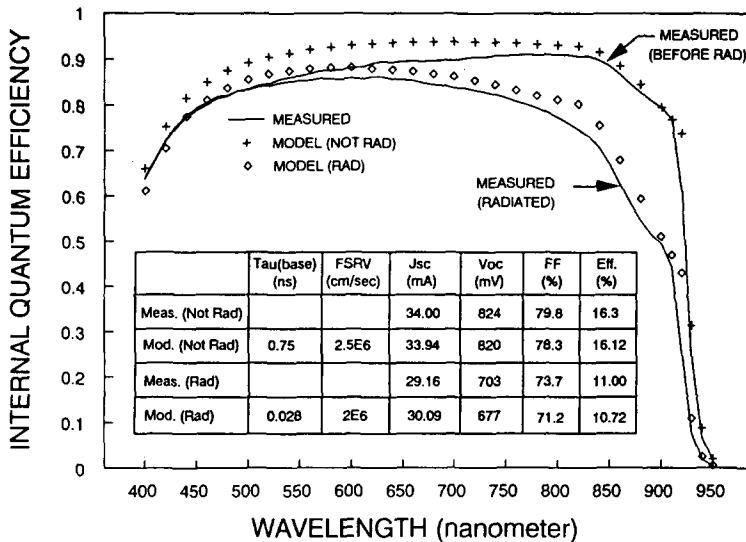


Fig. 2. Comparison of measured and calculated quantum efficiency and cell data before and after irradiation of n^+-p InP solar cell with a base doping of $2 \times 10^{16} \text{ cm}^{-3}$.

odology is improved for silicon and GaAs cells, where material parameters used in models are known more accurately.

3. Promising techniques for characterizing radiation-induced defects in semiconductors

Cell data, spectral response and lifetime measurements help in the assessment of radiation-induced damage to solar cells. However, they do not provide any insight and information about the defects responsible for that damage. This section briefly describes three techniques that are frequently used to reveal and quantify the defects generated by high energy radiation in semiconductors.

3.1. Deep level transient spectroscopy (DLTS)

DLTS is one of the most popular techniques because it is capable of providing information about the energy level, density, and capture cross-section of the traps, induced by high energy radiation. In a $p-n$ junction solar cell, one can determine majority as well as minority carrier traps by tailoring the bias conditions during the measurements.

DLTS is a capacitance transient technique in which the transients are generated from deep levels or traps by applying voltage pulses repetitively to a reverse-biased depletion region of the device. This technique is well documented in the literature [8–10]. Different experimental arrangements have been used for DLTS measurements. Lang [9] used a double-boxcar integrator to process the capacitance transients; Miller [8] introduced an

optimized correlator; and Kimerling [10] used a lock-in amplifier for signal integration. The DLTS system described in this paper [11] (Fig. 3), is similar to Kimerling's lock-in amplifier set-up. The use of a track-and-hold circuit in this set-up smoothly eliminates the transients due to bias pulses and the lock-in phase setting is kept at zero. The measurement set-up also includes a time-base generator which provides three signals: a reference signal for the lock-in amplifier, a hold signal for the sample-and-hold module, and a trigger signal for the pulse generator.

Figure 4 illustrates in four steps how capacitance transients are generated from the traps present in a solar cell junction. Step 1 shows a reverse-biased device which, in step 2, is pulsed to fill the traps in the depletion range. At the end of the pulse, step 3, the device capacitance does not return to its original value because of the trapped charges (electrons in this example) at the deep level. At temperatures where sufficient excitation energy is present,

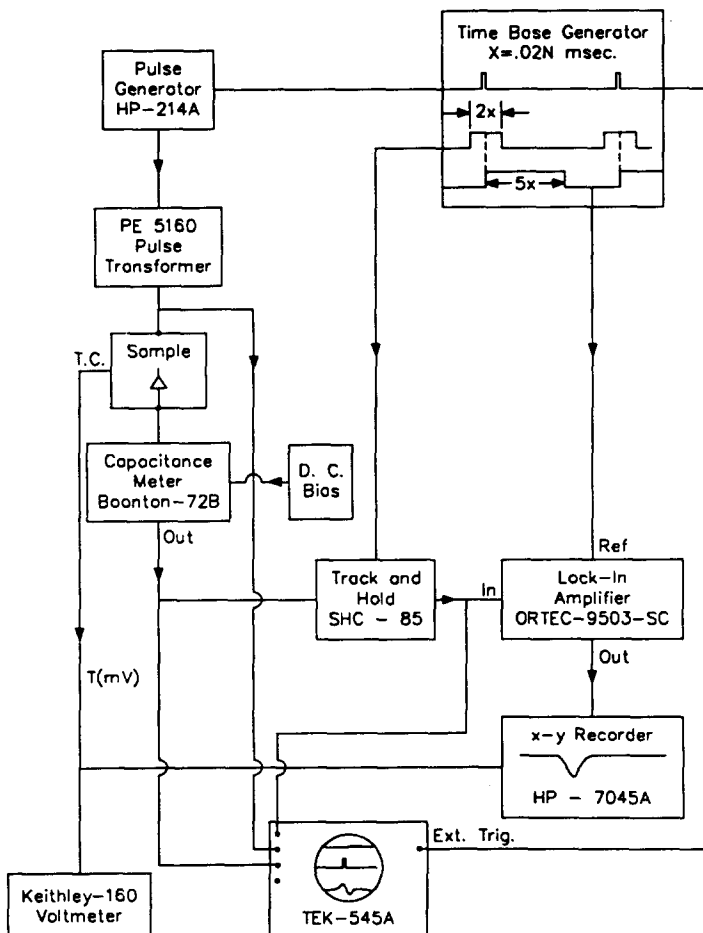


Fig. 3. Schematic diagram of the DLTS apparatus [11].

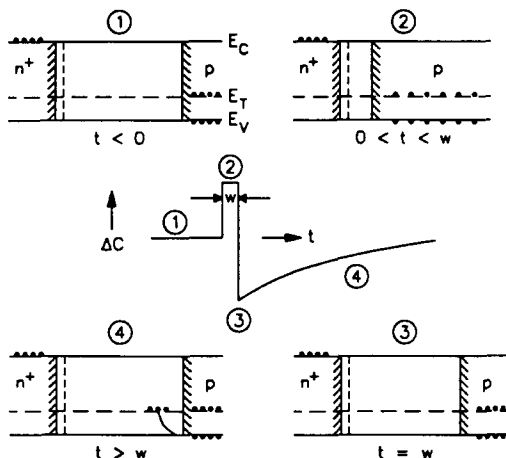


Fig. 4. Capacitance transient due to majority carrier trap in $n^+ - p$ diode. Steps 1 to 4 schematically show the charge state of the defect in the space charge region, between the shaded edges, before, during, and after the bias pulse.

these trapped charges are released by thermal emission during the period between the pulses, step 4, producing a capacitance transient. The device temperature is raised slowly from liquid nitrogen (or liquid helium) temperature to vary the emission rate of the trap or the time constant of the transient. These transients are processed with the help of a lock-in amplifier to provide an output signal as a function of device temperature, which passes through maxima or peaks indicating the presence of traps. The positions of these peaks are uniquely determined by the instruments' settings and the thermal emission properties of the respective traps. The proper choice of experimental parameters can give the activation energy, density and capture cross-section of each trap [8].

Figure 5 shows how the signals at various stations are related in the DLTS system shown in Fig. 3. The lock-in output L is given by

$$L = \frac{G_L}{T_B} \int_0^{T_B} S(t) W(t) dt \quad (1)$$

where $S(t)$ is the output of the sample-and-hold module;

$$S(t) = \begin{cases} K & \text{for } 0 < t < 0.1T_B \\ \Delta C_0 G_c \frac{\exp(-t - 0.1T_B + T_d)}{\tau} & \text{for } 0.1T_B < t < 0.9T_B \\ K & \text{for } 0.9T_B < t < T_B \end{cases} \quad (2)$$

Constant K represents the clamped signal value during the holding pulse. The output of track and hold circuit in Fig. 5 clearly shows that the signal is held constant during the time intervals $0 - 0.1T_B$ and $0.9T_B - T_B$. $W(t)$ is the lock-in reference signal or the weighting function:

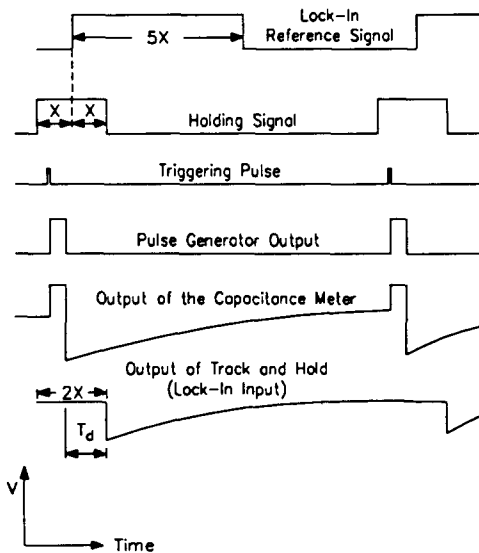


Fig. 5. Schematic diagram of the signals in the DLTS set-up [11].

$$W(t) = \begin{cases} +1 & \text{for } 0 < t < 0.5T_B \\ -1 & \text{for } 0.5T_B < t < T_B \end{cases} \quad (3)$$

ΔC_0 is the change in capacitance at the end of bias pulse; G_L and G_c are the gains of the lock-in amplifier and the capacitance meter, the delay time T_d is the interval between the end of the bias pulse and the end of the holding interval; and the repetition period of time base T_B is equal to $10X$ in Fig. 5. Equations (1)–(3) give

$$L = \frac{G_c G_L \tau \Delta C_0}{T_B} \exp\left(-\frac{T_d}{\tau}\right) \left[1 - \exp\left(-\frac{T_d}{2\tau}\right)\right]^2 \quad (4)$$

where $T_e = 0.8T_B$, and τ is the inverse of emission rate at that temperature.

The time constant τ_p at the maximum output is obtained from

$$\frac{dL}{d\tau} = 0 = \left(1 + \frac{T_d}{\tau_p}\right) - \left[\exp\left(-\frac{T_e}{2\tau_p}\right)\right] \left[\frac{T_e}{\tau_p} + \left(1 + \frac{T_d}{\tau_p}\right)\right] \quad (5)$$

Equation (5) can be solved for τ_p with the help of a computer program using Newton's method.

Thus, the emission rate $e = 1/\tau_p$ at the peak temperature T_M is fixed by the choice of T_B and T_d . The emission rate is given by [8]

$$e = \frac{N_c \sigma V_{th}}{g} \exp\left(\frac{\Delta E}{KT}\right) \quad (6)$$

The product $N_c V_{th}$ is proportional to T^2 , so that if the capture cross-section σ is temperature independent, the activation energy ΔE of the trap

can be obtained from the Arrhenius plot of e/T_m^2 vs. $1/T_m$, and the intercept gives the capture cross-section σ_0 .

The trap density N_t is obtained by first calculating ΔC_0 from the measured value of L at $\tau = \tau_p$ (eqn. (4)) and then using the following equation, which is valid for uniform doping and $N_t \ll N_A - N_D$

$$N_t = 2 \frac{\Delta C_0}{C} (N_A - N_D) \quad (7)$$

where $N_A - N_D$ is the net doping and C is the capacitance of the reverse-biased device.

The capture cross-section σ of the trap at the peak temperature can also be determined by shrinking the width of the injection pulse to fill the traps only partially. The slope of $\ln[(N_{t0} - N_t)/N_{t0}]$ (fraction of unfilled traps) vs. pulse width gives the capture rate c from which σ can be obtained at peak temperature according to

$$N_t = N_{t0}(1 - e^{-ct}) \quad (8)$$

$$c = n\sigma V_{th} \quad (9)$$

where N_{t0} is the total number of traps, N_t is the number of filled traps, t is the pulse width, n is the injected carrier concentration and V_{th} is the thermal velocity at the peak temperature.

3.2. Positron annihilation spectroscopy (PAS)

Positron annihilation spectroscopy is a nondestructive technique which can be used to characterize the radiation-induced atomic defect structures in semiconductors. PAS experiments have been used to study radiation damage in semiconducting materials due to laser, electron, proton, gamma and neutron irradiation. They have also been used to investigate the annealing behavior of the corresponding defects.

When a positron encounters an electron, the two particles annihilate to produce two γ -rays. If both particles were at rest, conservation of momentum and energy would require the two γ -rays, each with an energy of 511 keV, to be emitted in exactly opposite directions. The finite momentum of the electron/positron pair in the material, however, modifies the characteristics of the annihilation radiation. The technique which measures the deviations from 180° is called angular correlation and the method which measures the energy deviations from 511 keV is known as Doppler-broadened PAS.

In a typical experiment, positrons are injected from a radioactive source (e.g. ^{22}Na or ^{68}Ge) and quickly reach thermal velocities. Since the momentum of the thermalized positron represents less than 5% of the momentum of the least energetic electrons in the sample, the measured changes in the annihilation radiation characteristics reflect the electron momentum distribution in the vicinity of the lattice position at which the annihilation event occurred [12]. Since positrons can be preferentially attracted to, and become localized within, open volume and/or negatively charged defect sites, changes

in the relative concentrations of such sites will influence the observed annihilation energy characteristics.

A typical annihilation energy distribution function is shown in Fig. 6. This function can be modeled as the sum of an inverted parabola, representing annihilation events with comparatively low energy valence electrons, and a broader Gaussian distribution, representing annihilation events with core electrons. When a positron becomes localized within an open volume defect, the relative probability of annihilation with a core electron decreases. The reduction in the number of annihilation events with the comparatively high momentum core electrons (*i.e.* large energy shift events) reduces the width of the energy spectrum.

Doppler PAS energy distributions are usually interpreted using a characteristic lineshape parameter S defined as the sum of the counts in an arbitrarily selected central region of the peak divided by the total number of counts in the annihilation energy spectrum [13]. In general, the electron momentum distribution in the defect region will be narrower than in the bulk (*i.e.* $S(\text{defect}) > S(\text{bulk})$).

The measured S parameter is the weighted sum of the S parameters in the bulk and those of all of the different classes of defects in the sample

$$S_m = f_b S_b + \sum_i f_i S_i \quad (10)$$

where the subscripts m and b refer to the measured and bulk values; the f s are the fraction of positrons annihilating from each type of defect state, and the summation is carried out over all defect types. This analysis is most useful when there is a single dominant defect type, in which case

$$S_m = (1 - f_t) S_b + f_t S_t \quad (11)$$

where the subscript t refers to the trapped (defect) state. Since S_t is usually greater than S_b , but both are constant, an increase in S_m suggests an increase in f_t , which corresponds to an increase in the defect concentration.

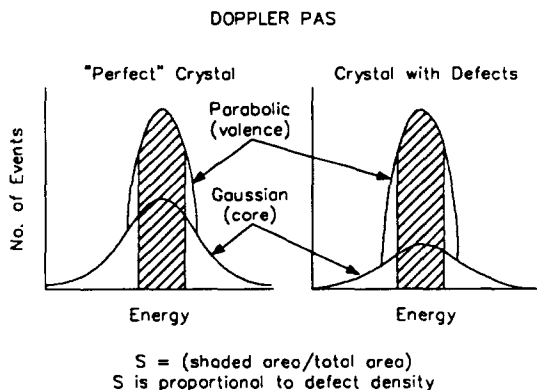


Fig. 6. A schematic representation of the Doppler PAS annihilation energy spectrum showing the contributions from core and valence electrons.

Using another version of PAS, known as the lifetime technique, it is possible to characterize multiple defect types simultaneously and determine their relative densities. Defect identification is accomplished by accurately determining the lifetime of the positron when it becomes spatially localized within a specific defect. The positron lifetime depends on the concentration of electrons in the region in which the annihilation event occurs (*i.e.* it will be characteristic of the trapping site). These measurements employ ^{22}Na as a source material since it simultaneously emits a γ -ray along with the positron. This γ -ray acts to start the timing apparatus which is stopped by the arrival of the annihilation γ -ray.

Lifetime PAS results are interpreted by fitting the raw data using an equation of the form

$$N(t) = \sum_i I_i \exp(-t/\tau_i) \quad (12)$$

where I_i and τ_i are known, respectively, as the measured intensities and lifetimes. The functional form of the relationship between the measured parameters and properties of interest (defect identification and defect densities) depends on the trapping model used to interpret the data. The majority of the PAS lifetime experiments are interpreted using the simple trapping model (STM) [14, 15]. The STM can be summarized as follows. At any time t , there will be $N_b(t)$ thermalized positrons present in the bulk regions of the host lattice. These positrons will annihilate with a characteristic rate λ_b . Additionally, some of the positrons will be trapped by lattice defects at a rate K_d which is characteristic of the defect involved and proportional to the defect density. The positrons trapped at such defect sites, $N_d(t)$, will annihilate at a rate λ_d . These assumptions lead to a set of coupled differential equations which can be solved to yield

$$N(t) = [N_0/(\lambda_b - \lambda_d + K_d)] \{K_d \exp(-\lambda_d t) + (\lambda_b - \lambda_d) \exp[-(\lambda_b + K_d)t]\} \quad (13)$$

Comparing this equation with eqn. (12), with $i=2$, yields expressions for the quantities of interest (λ_d and K_d) in terms of the measured quantities (I_1 , I_2 , λ_1 and λ_2). For example, the appropriate expression for K_d is

$$K_d = I_2[(1/\tau_1) - (1/\tau_2)] \quad (14)$$

Thus, K_d , and hence defect concentration, can be investigated using lifetime PAS. Although the mathematics becomes more complex, it is possible to extend this analysis to include more than one type of defect.

In order for lifetime PAS to be useful, one must have available a listing of the various radiation-induced defect types and their associated signature lifetimes. In this respect, defect identification by lifetime PAS is similar to the DLTS technique where one needs a library of deep levels to identify a trap. Table 1 shows positron lifetimes associated with the types of defects generated in silicon by radiation [16–22].

One of the drawbacks of using conventional positron sources is that one is limited to the investigation of the average defect density in a region which extends from the specimen surface down to $\approx 100 \mu\text{m}$ below the

TABLE 1

PAS lifetime values in silicon (from refs. 16–22)

Defect	Lifetime (ps)
Bulk	222 ± 2
Monovacancy	266 ± 10
Divacancy	325 ± 20
Quadrivacancy	435 ± 30
Hexavacancy	≈ 525
Oxygen interstitials	≈ 100
Oxygen-vacancy complexes	≈ 240

sample surface. This is a consequence of the wide spread in initial kinetic energies of positrons emitted from such sources. If depth resolution is important, then a beam characterized by a narrow energy distribution is required. The technique which utilizes a beam is known as slow (or thermal) PAS [23–25].

3.3. *Electron paramagnetic resonance (EPR)*

EPR refers to the resonant absorption of electromagnetic radiation by a system composed of unpaired electrons placed in a magnetic field [26, 27]. The technique can be used to investigate the electronic structure of radiation-induced point defects. EPR has been extremely useful for characterizing defects in silicon [28–34]. The primary reason for this success is that while a perfect crystal of diamagnetic silicon would not be expected to respond to an external magnetic field, the existence of point defects can result in local paramagnetic regions of the crystal. In contrast, the interpretation of EPR data for the III–V compounds is more difficult due to the larger fraction of atoms in the bulk with nuclear spins.

The EPR experiment involves placing a sample in a cavity and applying an alternating magnetic field of frequency ω . The introduction of a sample with susceptibility $\chi = \chi' - i\chi''$ changes the inductance and the resistance of the cavity. The change in resistance ΔR is given by $(\Delta R/R_0) = 4\pi\chi''Q$, where $Q = L_0\omega/R_0$ is known as the quality factor. By measuring the loss of the quality factor Q , as a function of ω , one can detect resonance. In practice, it is difficult to vary frequency, therefore ω is kept constant and the magnitude of the magnetic field is varied.

By varying the orientation of the applied magnetic field with respect to the crystallographic orientation of the sample, one can obtain information regarding the geometrical shape of the defect. For example, tetrahedral coordination can be recognized. The external magnetic field is, however, not the only magnetic field with which the unpaired electrons can interact. For instance, one must consider the magnetic coupling of the electron to the nearby nuclei. The study of this kind of interaction, termed hyperfine interaction, is an extremely powerful method to identify the nature of the atom involved in a defect.

4. Selected applications of DLTS, PAS and EPR

4.1. Characterization of irradiation-induced defects by DLTS

Selected examples from the literature will be used to illustrate the application of the above techniques in understanding and revealing the radiation-induced defects and their annealing behavior. Irradiation of semiconductors with high energy electrons generates Frenkel defects in the lattice. Some of the vacancies and interstitials are mobile enough to avoid recombination and interact with other defects and dopant atoms, resulting in various defect complexes.

4.1.1. DLTS on irradiated *p*-silicon

Rohatgi [35] showed by DLTS measurements (Fig. 7(a)) that 1 MeV electron irradiation ($5 \times 10^{15} \text{ e cm}^{-2}$) of an n^+p , boron-doped, float zone silicon solar cell gives rise to five deep levels at $E_c - 0.17 \text{ eV}$, $E_c - 0.24 \text{ eV}$, $E_v + 0.21 \text{ eV}$, $E_v + 0.31 \text{ eV}$ and $E_v + 0.37 \text{ eV}$. By tracking the cell recovery and change in concentration of various deep levels as a function of annealing temperature (Fig. 7(b)), Rohatgi was able to show that the deep level at $E_v + 0.31 \text{ eV}$ is responsible for the cell degradation and reverse annealing, because of which high temperatures are required to anneal out the radiation damage in boron-doped silicon. He found that the $E_v + 0.31 \text{ eV}$ level starts to grow at an annealing temperature of $\approx 150^\circ\text{C}$ and eventually anneals out at $\approx 400^\circ\text{C}$. Similar results were previously reported by Weinberg [36] for boron-doped n^+p Czochralski solar cells using DLTS technique.

The above DLTS results prompted the idea of introducing dopants which would not form electrically active defects. Wienberg *et al.* [37] demonstrated that gallium-doped silicon indeed shows (a) more rapid recovery during post-

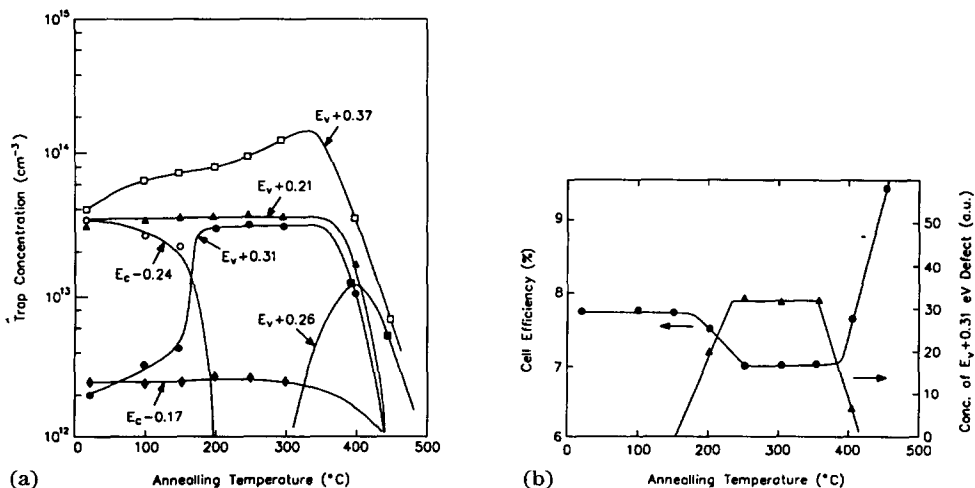


Fig. 7. (a) Change in defect concentrations during isochronal anneal of electron-irradiated ($5 \times 10^{15} \text{ e cm}^{-2}$) float zone silicon cell. (b) Relationship between the annealing behavior of $E_v + 0.31 \text{ eV}$ defect and reverse annealing of electron-irradiated web solar cell.

irradiation anneal, relative to comparable boron-doped silicon, and (b) no severe reverse annealing effects.

4.1.2. DLTS on irradiated-*p*-InP

Ando *et al.* [38] fabricated n^+-p InP solar cells by diffusion of sulphur into *p*-type substrates containing $1 \times 10^{16} \text{ cm}^{-3}$ Zn. These cells were irradiated with 1 MeV electrons. DLTS measurements showed the formation of two levels, H4 and H5, at $E_v + 0.37 \text{ eV}$ and $E_v + 0.52 \text{ eV}$, respectively, in *p*-InP. Figure 8 shows that the deep level H4, with activation energy of 0.37 eV, disappeared under successive photo-injections or forward-biased carrier injections at or below room temperature.

From the Arrhenius plots of H4 center annealing rates (τ^{-1}/s^{-1}), determined by DLTS, for both thermal and injection enhanced annealings, an activation energy of 1.14 eV was obtained for the thermal annealing process. However, a small activation energy (about 0.14 eV) was observed under minority-carrier injection in the low temperature region (Fig. 9). Hence, forward-biased injection or photo-injection seem to reduce defect annealing activation energy which results in low temperature defect migration and annealing of the major H4 center at low temperature.

In addition, the difference between the activation energies for thermal and injection annealings corresponds to the energy emitted from the elec-

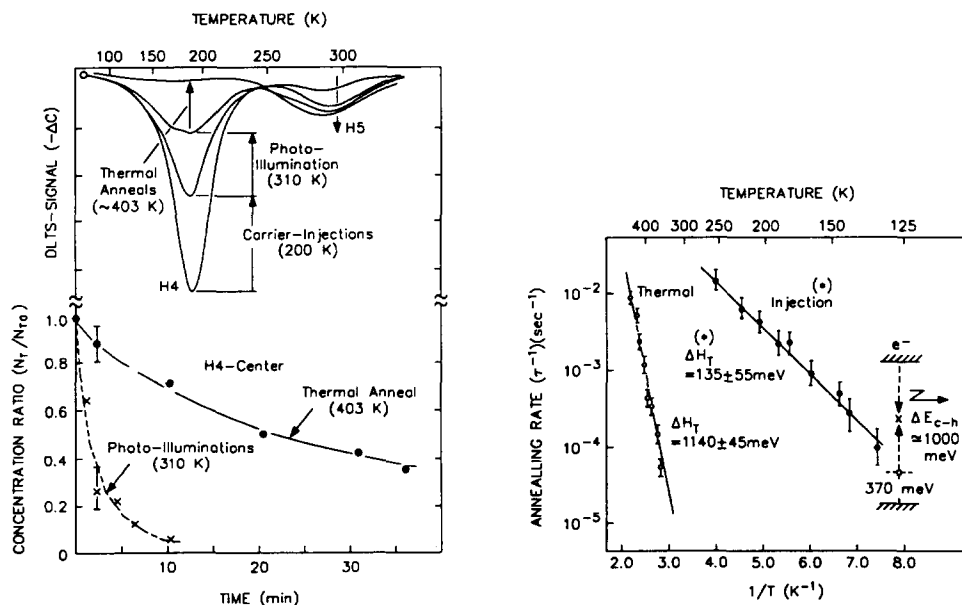


Fig. 8. DLTS spectra for irradiation induced deep hole traps in *p*-type InP. Shown also are successive annealings by forward-biased-minority carrier injection, photo-injection and thermal annealing in a *p*-type layer of n^+-p junction solar cells [38].

Fig. 9. Annealing rate vs. $1/T$ plots for the H4 center under thermal annealing around 400 K and forward-biased injection annealing in low temperatures [38].

tron-hole recombination process at the H4 center [38] as shown in Fig. 9. This suggests that minority carrier injection annealing originates from non-radiative electron-hole recombination at the H4 center in *p*-InP. This is the so-called recombination enhanced defect reaction (REDR) effect. Thus, DLTS measurements were able to reveal why InP solar cells are radiation hard and why the radiation-induced defects in *p*-InP can be annealed at room temperature under forward bias and photo-illumination.

4.2. Characterization of defects by PAS in neutron-irradiated silicon

Dannefaer *et al.* [39] applied the PAS technique to identify and investigate the annealing behavior of defects formed by neutron radiation of silicon. Lifetime PAS measurements showed two positron lifetimes; $\tau_1 = 226$ ps with intensity $I_1 \approx 76\%$ and $\tau_2 = 325$ ps with $I_2 = 24\%$ after neutron irradiation [39]. According to Table 1, $\tau_1 \approx 226$ ps is associated with bulk silicon while $\tau_2 = 325$ ps corresponds to positrons trapped at divacancies in silicon. Figure 10 shows the change in τ_2 and I_2 after 20 min isochronal anneals. Based on the annealing behavior, Dannefaer divided the annealing range into three stages. Stage I (30–150 °C), where τ_2 remains unchanged but I_2 decreases from 24 to 7%, reflects the annealing of divacancies via migration of interstitials [39]. Stage II (150–250 °C) is characterized by τ_2 having a new, approximately constant lifetime of 435 ps. This happens because divacancies can now migrate and form quadrivacancy. This is substantiated by the fact that increase in positron lifetime over the bulk lifetime value should be roughly proportional to the number of vacancies in the cluster or the size of the open volume. The increase in τ_2 in Stage II over the bulk is $435 - 225 = 210$ ps, which is approximately twice the increase for divacancy $325 - 225 = 100$ ps, suggesting quadrivacancy formation.

The decrease in τ_2 beyond 260 °C in Stage III was interpreted as the result of break-up of quadrivacancy complex. At 340 °C, τ_2 again becomes close to the divacancy lifetime of 325 ps. An increase in τ_2 and the decrease in I_2 beyond 340 °C is the result of break-up of divacancies because it follows a first-order process with an activation energy of 1.7 eV, which agrees well with the binding energy of divacancies [39]. This example shows clearly

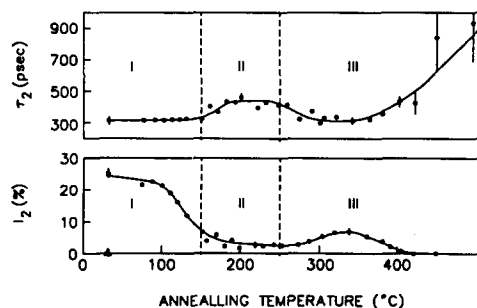


Fig. 10. Defect lifetime τ_2 and intensity I_2 after 20 min isochronal anneals. The vertical dotted lines separate the annealing stages I, II and III [39].

how PAS can provide a more detailed picture of defects and their annealing behavior, specially when the defects associated with measured positron lifetimes are known.

4.3. Characterization of defects by EPR in irradiated *p*-type silicon

To demonstrate the wealth of information that can be obtained from EPR measurements, consider the investigation of the radiation-induced Si-A center [28]. Watkins and Corbett used EPR to identify this defect as a lattice vacancy containing an oxygen atom bridging two of the four broken bonds. They pointed out that the spin resonance and electrical activity resulted from an electron trapped by the remaining two bonds. The hyperfine interaction with the ^{29}Si ($\approx 5\%$ abundant) revealed that the trapped electron was highly localized on two silicon atoms. Orientation studies showed the defect to have triangular symmetry. The proposed physical model for the defect is shown in Fig. 11.

EPR has been used successfully to characterize radiation-induced damage by energetic electrons in *p*-type silicon [26, 40]. A schematic representation of the raw data [26] attributed to a specific defect in silicon is shown in Fig. 12. The spectrum contains three equally intense main peaks, each of which is surrounded by four pairs of symmetrically distributed satellite peaks.

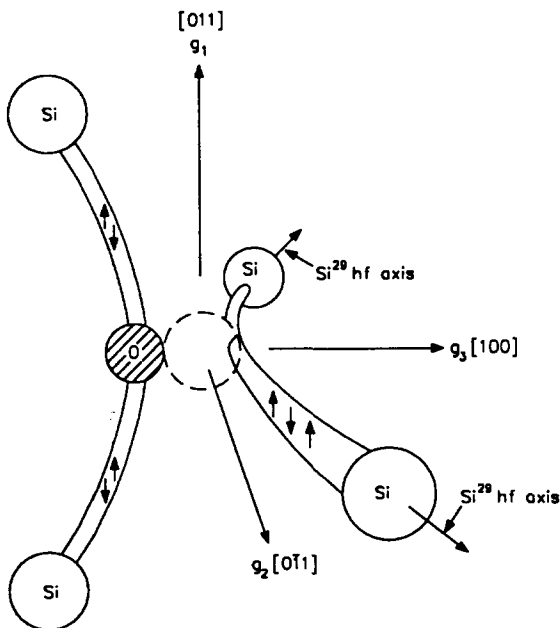


Fig. 11. Model of the A center as a substitutional oxygen atom. The oxygen atom bonds between two of the four neighboring silicon atoms, and the remaining two silicon atoms pull together to form a covalent bond. Spin resonance arises from an additional electron which is trapped in the Si-Si molecular bond as shown. The *g* tensor and hyperfine axes are indicated [28].

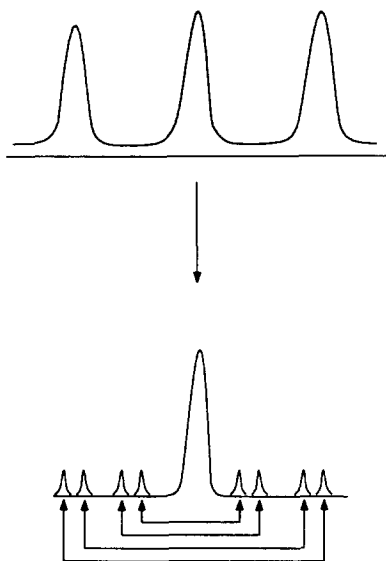


Fig. 12. A schematic representation of the EPR data for a V^+ defect in silicon [26]. The spectrum contains equally intense peaks. Bottom figure shows the central resonance of the triplet with its hyperfine structure splittings.

By changing the orientation of the external magnetic field with respect to the crystallographic orientation of the sample, it was found that the three central lines exhibited axial symmetry around a $\langle 100 \rangle$ direction. An orientation analysis of the hyperfine interaction (satellite peaks) reveals an axis of symmetry slightly shifted from a $\langle 111 \rangle$ direction.

Based on the primary peak information, it was concluded that the defect could exist with three nonequivalent, but equally populated, $\langle 100 \rangle$ orientations. The hyperfine interactions result from the naturally occurring ^{29}Si atoms. The existence of four pairs of satellites implies four types of silicon atoms in the vicinity of the defect. The slight shift in the symmetry axis from $\langle 111 \rangle$ reflects a local distortion of the lattice in the vicinity of the defect. From this analysis, it was postulated that the defect was a vacant silicon site containing an odd number of electrons. A more quantitative analysis of the data resulted in the conclusion that the defect was positively charged vacancy V^+ .

Acknowledgments

The authors would like to acknowledge the support of EPRI, Contract #RP-8004, for the PAS technique development and its applications.

References

- 1 A. Yamamoto, M. Yamaguchi and C. Uemura, *Appl. Phys. Lett.*, **44** (1984) 611.
- 2 M. Yamaguchi, K. Ando, A. Yamamoto and C. Uemura, *Appl. Phys. Lett.*, **44** (1984) 432.
- 3 C. J. Keavney, V. E. Haven and S. M. Vernon, *Conf. Rec. 21st, IEEE Photovoltaic Specialists' Conf.*, 1990, IEEE Inc., New York, p. 141.
- 4 J. Mandelkorn, C. McAfee, J. Kesperis, L. Schwartz and W. Pharo, *J. Electrochem. Soc.*, **109** (1962) 313.
- 5 I. Weinberg, C. K. Swartz and R. E. Hart, *Conf. Rec. 18th IEEE Photovoltaic Specialists' Conf.*, 1985, IEEE Inc., New York, p. 1722.
- 6 N. D. Arora, S. G. Chamberlain and D. J. Roulston, *Appl. Phys. Lett.*, **37** (1980) 325.
- 7 P. A. Basore, *Proc. Sixth Biennial University/Government/Industry Microelectronics Symp.*, p. 73, 1985.
- 8 G. L. Miller, D. V. Lang and L. C. Kimerling, *Ann. Rev. Mater. Sci.*, Vol. 7, (1977) 377.
- 9 D. V. Lang, *J. Appl. Phys.*, **45** (1974) 3023.
- 10 L. C. Kimerling, *IEEE Trans. Nucl. Sci.*, **23**(6) (1976) 1497.
- 11 A. Rohatgi, J. R. Davis, R. H. Hopkins and D. G. McMullin, *Solid-State Electron.*, **26**(11) (1983) 1039.
- 12 C. F. Coleman, *NDT International*, **10** (1977) 227.
- 13 I. K. MacKenzie, J. A. Eady and B. R. Gingerich, *Phys. Lett.*, **33A** (1970) 279.
- 14 B. Bergsen and M. J. Stott, *Solid State Commun.*, **7** (1970) 1203.
- 15 D. C. Conners and R. N. West, *Phys. Lett. A*, **30** (1969) 24.
- 16 S. Dannefaer and D. Kerr, *J. Appl. Phys.*, **60** (1986) 1313.
- 17 P. Mascher, D. Kerr and S. Dannefaer, *Phys. Rev. B*, **35** (1987) 3043.
- 18 S. Dannefaer and D. Kerr, *J. Appl. Phys.*, **60** (1986) 591.
- 19 S. Dannefaer, G. W. Dean, D. P. Kerr and B. G. Hogg, *Phys. Rev. B*, **14** (1976) 2709.
- 20 S. Dannefaer, N. Fruensgaard, S. Kupca, B. Hogg and D. Kerr, *Can. J. Phys.*, **61** (1983) 451.
- 21 Y. J. He, M. Hasegawa, R. Lee, S. Berko, D. Adler and A. L. Jung, *Phys. Rev. B*, **33** (1986) 5924.
- 22 S. Dannefaer, S. Kupca, B. G. Hogg and D. P. Kerr, *Phys. Rev. B*, **22** (1980) 6135.
- 23 K. G. Lynn and H. Lutz, *Rev. Sci. Instrum.*, **51** (1980) 977.
- 24 A. Vehanen, K. G. Lynn, P. J. Schultz and M. Eldrup, *Appl. Phys.*, **A32** (1983) 163.
- 25 K. G. Lynn, B. Nielsen and J. H. Quatman, *Appl. Phys. Lett.*, **47** (1985) 239.
- 26 J. Bourgoin and M. Lannoo, *Point Defects in Semiconductors II*, Springer-Verlag Series in Solid-State Physics, Vol. 35, 1983.
- 27 C. P. Slichter, *Principles of Magnetic Resonance*, Harper and Row, New York, 1963.
- 28 G. D. Watkins and J. W. Corbett, *Phys. Rev.*, **121** (1961) 1001.
- 29 K. L. Brower, *Phys. Rev. B*, **4** (1971) 1968; **5** (1972) 4274; **14** (1976) 872.
- 30 Y. H. Lee, J. W. Corbett and K. L. Brower, *Phys. Status Solidi A*, **41** (1977) 637.
- 31 P. M. Lenahan and P. V. Dressendorfer, *J. Appl. Phys.*, **55** (1984) 3495.
- 32 M. Stutzmann, *Z. Phys. Chem. Neue Folge*, **151** (1987) 211.
- 33 P. M. Lenahan, W. L. Warren, P. V. Dressendorfer and R. E. Mikawa, *Z. Phys. Chem. Neue Folge*, **151** (1987) 235.
- 34 Y. Y. Kim and P. M. Lenahan, *J. Appl. Phys.*, **64** (1988) 3551.
- 35 A. Rohatgi, *Proc. 4th Solar Cell High Efficiency and Radiation Damage Conf.*, NASA-Lewis Research Center, Cleveland, Ohio, p. 281, 1980.
- 36 I. Weinberg and C. K. Swartz, *Appl. Phys. Lett.*, **36** (1980) 693.
- 37 I. Weinberg, H. W. Brandhorst, C. K. Swartz and S. Mehta, *Proc. 3rd European Symp. on Photovoltaic Generators in Space*, p. 89 (ESA, Noordwijk, The Netherlands, 1982).
- 38 K. Ando, M. Yamaguchi, A. Yamamoto and C. Uemura, *Conf. Rec. 18th IEEE Photovoltaic Specialists' Conf.*, 1985, IEEE Inc., New York, p. 770.
- 39 S. Dannefaer, G. W. Dean, D. P. Kerr and B. G. Hogg, *Phys. Rev. B*, **14** (1976) 2709.
- 40 G. D. Watkins, *J. Phys. Soc. Jpn.*, **18** (suppl. 2) (1963) 22.